JACS Au
AN OPEN ACCESS JOURNAL OF THE AMERICAN CHEMICAL SOCIETY

Open Access

This article is licensed under CC-BY-NC-ND 4.0

# Computational Reverse Engineering Analysis of the Scattering Experiment Method for Interpretation of 2D Small-Angle Scattering Profiles (CREASE-2D)

Sri Vishnuvardhan Reddy Akepati,[⊥] Nitant Gupta,[⊥] and Arthi Jayaraman[*]

Cite This: *JACS Au* 2024, 4, 1570−1582

Read Online

ACCESS | Metrics & More | Article Recommendations | SI Supporting Information

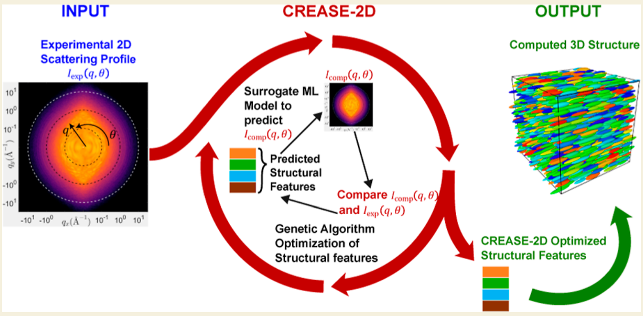
INPUT
CREASE-2D
OUTPUT
Experimental 2D Scattering Profile
$I_{exp}(q,\theta)$
$q$
$\theta$
$q_y(\text{Å}^{-1})$
$q_x(\text{Å}^{-1})$
$10^1$
$10^0$
$10^{-1}$
$-10^0$
$-10^1$
Surrogate ML Model to predict $I_{comp}(q,\theta)$
$I_{comp}(q,\theta)$
Predicted Structural Features
Compare $I_{comp}(q,\theta)$ and $I_{exp}(q,\theta)$
Genetic Algorithm Optimization of Structural features
Computed 3D Structure
CREASE-2D Optimized Structural Features

ABSTRACT: Small-angle scattering (SAS) is a widely used characterization technique that provides structural information in soft materials at varying length scales (nanometers to microns). The output of an SAS measurement is the scattered intensity $I(\mathbf{q})$ as a function of $\mathbf{q}$, the scattered wavevector with respect to the incident wave; the latter is represented by its **magnitude** $|\mathbf{q}| \equiv q$ (in inverse distance units) and **azimuthal angle** $\boldsymbol{\theta}$. While isotropic structural arrangement can be interpreted by analysis of the azimuthally averaged one-dimensional (1D) scattering profile, to understand anisotropic arrangements, one has to interpret the two-dimensional (2D) scattering profile, $I(q, \theta)$. Manual interpretation of such 2D profiles usually involves fitting of approximate analytical models to azimuthally averaged sections of the 2D profile. In this paper, we present a new method called CREASE-2D that interprets, without any azimuthal averaging, the entire 2D scattering profile, $I(q, \theta)$, and outputs the relevant structural features. CREASE-2D is an extension of the "computational reverse engineering analysis for scattering experiments" (CREASE) method that has been used successfully to analyze 1D SAS profiles for a variety of soft materials. CREASE-2D goes beyond CREASE by enabling analysis of 2D scattering profiles, which is far more challenging to interpret than the azimuthally averaged 1D profiles. The CREASE-2D workflow identifies the structural features whose computed $I(q, \theta)$ profiles, calculated using a surrogate XGBoost machine learning model, match the input experimental $I(q, \theta)$. We expect that this CREASE-2D method will be a valuable tool for materials' researchers who need direct interpretation of the 2D scattering profiles in contrast to analyzing azimuthally averaged 1D $I(q)$ vs $q$ profiles that can lose important information related to structural anisotropy.

KEYWORDS: *small-angle scattering, 3D structure, computational analysis, two-dimensional scattering profile, CREASE, XGBoost, genetic algorithms*

Researchers studying soft materials, namely, polymers, colloids, liquid crystals, gels, and chemical formulations, aim to establish molecular design−structure−property relationships to engineer new materials with improved physical properties. Toward this goal, microscopy and scattering are two prominent characterization techniques for understanding the structure formed within such soft materials. Microscopy techniques that are commonly used for soft materials include optical microscopy to probe structures with length scales above 10 $\mu$m and scanning electron/transmission electron/atomic force microscopy (SEM/TEM/AFM) to probe structures with features below 10 $\mu$m. Such microscopy methods can reveal the pertinent structural features in the area of the material that is imaged, albeit only over a narrow range of length scales. Furthermore, microscopy only outputs a two-dimensional (2D) projection of the structure and the depth information can be nontrivial to interpret. In contrast, bulk structural characterization techniques that rely on scattering of light (X-rays/visible/infrared) or neutrons are able to reveal three-dimensional (3D) structural information across multiple length scales. In particular, for soft materials, small-angle X-ray scattering (SAXS) and small-angle neutron scattering (SANS) techniques[1−8] are used widely to elucidate spatial distributions of amorphous (i.e., not crystalline) ordered or disordered structures at various length scales.

A typical SAXS or SANS measurement captures the **scattered intensity** $\boldsymbol{I}(\mathbf{q})$ as a function of the scattered wavevector $\mathbf{q}$ with respect to the incident wave, expressed by its **magnitude** $|\mathbf{q}| \equiv q$ (in inverse distance units) and the **azimuthal angle** $\boldsymbol{\theta}$. For materials that have isotropic structural

Received: January 22, 2024
Revised: March 1, 2024
Accepted: March 5, 2024
Published: March 20, 2024

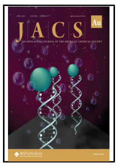

ACS Publications

© 2024 The Authors. Published by American Chemical Society

https://doi.org/10.1021/jacsau.4c00068

arrangements, the patterns found in the 2D SAXS/SANS profiles, $I(q, \theta)$, are expected to exhibit a spherical or cylindrical symmetry. The analysis of such symmetric scattering profiles involves integrating over all azimuthal angles and fitting analytical models to the one-dimensional (1D) form of the scattering profile—$I(q)$ vs $q$. The presence of a peak in these 1D scattering profiles at a certain $q$ value indicates the presence of structural correlations at length scales around $2\pi/q$, either due to the dimensions of the constituent particles [i.e., form factor, $P(q)$] or the arrangement of particles that influences their interparticle spacing [i.e., structure factor, $S(q)$]. Therefore, even when a structure consists of anisotropic particles that are devoid of any interparticle orientational order, the 1D scattering profile can reveal most of the relevant structural details about the material. Furthermore, in the case of dilute solutions (e.g., amphiphilic polymer solutions at low polymer concentrations), the form factor of the primary particle (e.g., assembled micelles) can be analyzed using shape-dependent or shape-independent models to obtain the dimensions of the primary particles.[9] However, in cases where there is significant dispersity in dimensions of the primary particles, such models can be poor approximations, and the resulting analysis can be flawed. In the case of concentrated solutions (e.g., amphiphilic polymer solutions at high concentrations), in addition to the form factor of the primary particle, one has to analyze the structure factor which holds the information about spatial arrangement of the primary particles (e.g., interparticle or intermicelle arrangement). In such cases, if one assumes that the form factor remains constant with a changing concentration, then one can use the analyzed form factor obtained at dilute concentration to interpret the structure factor. Analytical structure factor models like the "sticky hard sphere" or "Percus−Yevick"[10] can be used to interpret isotropic structures with low dispersity. However, in the case of systems where the values of the primary particle's shape and size or entire distributions of the shape and size of primary particles change with concentration or systems in which the structure develops anisotropy during processing or rheological measurements;[11−13] the interpretation of these scattering profiles can be challenging.

To circumvent these challenges with traditional approaches involving manual fitting with shape-dependent or shape-independent models that can be approximate or incorrect in some cases, there is a need for other analysis approaches. Additionally, the surge in high-throughput measurements and the quest for artificial intelligence (AI)-driven manufacturing demand analysis methods that can be fast and automated in interpreting scattering profiles and complementary characterization results, as and when the measurement is done. We direct readers to a recent perspective by Anker et al. that covers many ongoing developments and studies within this topic of fast computational analysis of scattering and spectroscopic measurements in materials sciences.[14] The challenges for computational methods being developed for fast or automated scattering analyses in the area of synthetic soft materials are different from inorganic hard materials or biological molecules. This is because (nonbiological) soft material structures tend to be mostly amorphous, often exhibiting significant dispersity in structural dimensions, unlike the precise crystalline order seen in inorganic materials or secondary and tertiary structures of proteins,[15−17] To address this specific need in the area of soft materials with amorphous structures, Jayaraman and co-workers recently developed the "computational reverse engineering analysis of scattering experiments" (CREASE) method.[18−26]

The CREASE method outputs the features or descriptors of the 3D structures that produce "computed" scattering profiles, $I_{\text{comp}}(q)$, which closely resemble the scattering profile obtained in experiments, $I_{\text{exp}}(q)$. Rather than iterating exhaustively over 3D structures themselves, which can be a computationally intensive and slow process, in CREASE, the optimization cycle iterates over a lower dimensional representation of the 3D structures. We call these lower-dimensional descriptors of the structure as structural features; as we use the genetic algorithm (GA) for optimization, in the jargon of evolutionary algorithms, we refer to these structural features as "genes".

In a typical GA optimization loop, an initial population of "individuals" is generated where each individual has a unique set of structural features or "genes". The structural features can have single values of structural parameters or encode parameters representing distributions of structural parameters. For each individual, these structural features are converted to a computed scattering profile using a surrogate machine learning (ML) model. The computed scattering profile $I_{\text{comp}}(q)$ of each individual is then compared to the input scattering profile $I_{\text{exp}}(q)$. The extent of the match between $I_{\text{comp}}(q)$ and $I_{\text{exp}}(q)$ is calculated as a fitness value for that individual. After the fitness value has been calculated for all individuals in a generation, then a new "generation" of individuals is created based on the current generation's fitness ranking and genetic operations like "pairing" and "mutations".[27] As the optimization proceeds, with each new "generation", the individuals progressively exhibit better fitness values, i.e., improvement in the match between their $I_{\text{comp}}(q)$ and the input $I_{\text{exp}}(q)$. At the end of the GA cycle, upon convergence in fitness values, CREASE outputs multiple individuals (i.e., sets of structural features) that all have mutually similar scattering profiles that also match the input scattering profile. If the GA results consist of multiple distinct sets of structural features, then one would use either their domain knowledge or guidance for imaging techniques and/or molecular modeling and simulations to remove the "individual(s)" that are deemed unphysical and keep only those "individual(s)" that are physically possible.

Within the optimization loop, the use of surrogate ML models for calculation of $I_{\text{comp}}(q)$ for each individual has significantly accelerated the computational speed of CREASE. Traditionally, for 3D structures with known positional coordinates of each particle or constituents of each particle, one would use the computationally intensive Debye scattering equation to calculate scattering profiles. To accelerate this step of calculating $I_{\text{comp}}(q)$, in recent CREASE studies, Jayaraman and co-workers introduced the idea of using a surrogate ML model [e.g., artificial neural networks (ANNs)] that connects the structural features (i.e., lower dimensional representation of the 3D structure) to its $I_{\text{comp}}(q)$.[20,22,23] Using this ML-enhanced CREASE, one can interpret input scattering profiles fast and on modest computational resources, as described in refs 19, 20, and 23.

There have been multiple soft material systems where CREASE has been used successfully to analyze the 1D scattering profiles, and in many cases, CREASE has performed better than existing analytical models. For example, CREASE has been used to analyze the form factor of assembled structures in dilute solutions; for example, spherical micelles,[18] cylindrical micelles,[21,22] and vesicles[24] formed by novel polymers or macromolecules in solution. In these cases, the

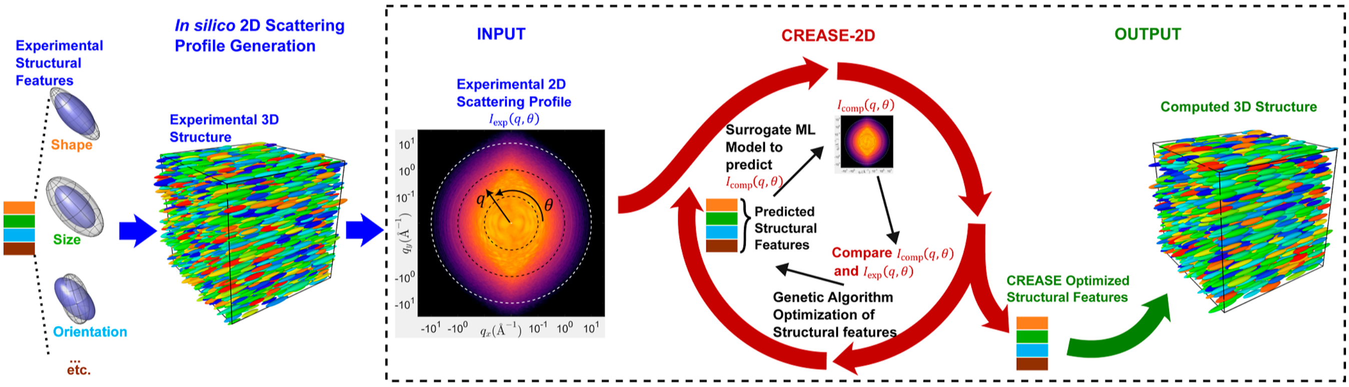
Experimental Structural Features
Shape
Size
Orientation
...
etc.
In silico 2D Scattering Profile Generation
Experimental 3D Structure
INPUT
Experimental 2D Scattering Profile
$I_{exp}(q,\theta)$
$q$
$\theta$
$q_y$ (Å$^{-1}$)
$q_x$ (Å$^{-1}$)
$10^1$
$10^0$
$10^{-1}$
$-10^0$
$-10^1$
CREASE-2D
Surrogate ML Model to predict $I_{comp}(q,\theta)$
$I_{comp}(q,\theta)$
Predicted Structural Features
Compare $I_{comp}(q,\theta)$ and $I_{exp}(q,\theta)$
Genetic Algorithm Optimization of Structural features
CREASE Optimized Structural Features
OUTPUT
Computed 3D Structure

**Figure 1.** CREASE-2D method workflow used in this paper. For proving the CREASE-2D works correctly, we used as the input an in silico 2D scattering profile generated from a 3D structure with a predefined set of structural features. Only the “experimental: 2D scattering profile, $I_{exp}(q, \theta)$ where $q$ is magnitude of scattered wavevector and $\theta$ is the azimuthal angle, is used as the input to the CREASE-2D method. The GA optimizes toward structural features whose $I_{comp}(q, \theta)$ closely resembles $I_{exp}(q, \theta)$. By comparing the optimized structural features to the ones used to create the $I_{exp}(q, \theta)$, we can show that CREASE-2D works well.

existing analytical models were either too approximate[18] or could not handle dispersity in structural dimensions well.[24] In some cases, CREASE was used to test hypotheses of potential assembled structures in the solution which could not have been done with analytical models alone.[28] CREASE has also been used to interpret the scattering profiles of concentrated particle systems where the form of the particle was known a priori (e.g., simple spherical particles); in this case, CREASE was used to understand the extent of mixing within binary nanoparticle mixtures.[20,25] CREASE has also been extended to the “$P(q)$ and $S(q)$ CREASE” version that can analyze both form and the structure factors of the primary particles simultaneously.[19] This “$P(q)$ and $S(q)$ CREASE” method was used to understand a system of silica particles coated with surfactant (core−shell particles) at varying temperature and salt concentrations. Both temperature and salts affect the cationic surfactants in the shell around the particles and as a result, the form of the surfactant-coated particles and interparticle structure.[29]

While all of the above applications of CREASE involved isotropic structures and the 1D scattering profile from experiments as the input, in this paper, we have extended the CREASE method to CREASE-2D that can analyze 2D scattering profiles directly and, in turn, enable interpretation of structures that may have anisotropy.

The input to CREASE-2D is a 2D scattering profile coming from structures that have some orientational order within the material’s structure either produced by processing conditions (e.g., shear or field-induced alignment of domains) and/or because of the form of primary particles (e.g., ellipsoidal domain). In such cases, characterization of structural anisotropy requires the use of the 2D SAS profiles, $I_{exp}(q, \theta)$, which hold information on the length scales of arrangements that can vary along various azimuthal angles, $\theta$.

In this paper, we present all relevant details of CREASE-2D method development and demonstrate its successful application by correctly outputting the structural features of the 3D structures that gave rise to the input in silico 2D scattering profile .

## CREASE-2D: OVERVIEW AND DEVELOPMENT

Figure 1 provides an overview of the CREASE-2D workflow presented in this paper. The overall development of CREASE-2D involves four key steps:

1. Generating a data set of 3D structures having an extensive variation of all important structural features. The structural features that we demonstrate in this study are distributions of domain sizes, shapes, orientational order, and volume fraction of domains that produce the scattering;
2. Computing the 2D scattering profiles for each of those 3D structures;
3. Using the combined data set of structural features and their computed 2D scattering to train the surrogate ML model that will output a computed scattering profile for an input of structural features; and
4. Incorporating the trained ML model within the GA optimization loop to fulfill the CREASE-2D workflow.

While step 4 above enables a smooth and fast execution of the CREASE-2D method, steps 1−3 are necessary for an accurate and reliable representation of experimentally relevant structural configurations and their scattering profiles. The amount and quality of data generated in steps 1 and 2 will also determine the accuracy of the surrogate ML model in step 3, which, in turn, dictates the efficacy of the CREASE-2D optimization. Before we describe each of the above steps in more detail, we note the similarities and differences between CREASE-2D and prior implementations of CREASE.

Similar to previous implementations, the CREASE-2D method also uses a GA to optimize structural features. The GA loop proceeds in a similar manner as in the previous uses of CREASE and stops when fitness of the individuals converges, i.e., an individual’s computed 2D scattering profile $I_{comp}(q, \theta)$ matches the input profile $I_{exp}(q, \theta)$. One difference between the previous CREASE implementation and CREASE-2D is in the choice of the surrogate ML model to calculate the $I_{comp}(q, \theta)$ for each individual. The surrogate ML model needed in this case needs to not only handle the input in the form of a table having multidimensional variation of its structural features but also to output a 2D scattering profile rather than a 1D scattering curve of $I_{comp}(q)$ vs $q$. More details are provided in the steps 3 and 4 subsections below.

### Step 1: Generating a Data Set of 3D Structures with Varying Structural Features

To develop a reliable surrogate ML model for linking structural features to the 2D scattering profile, we need a training data set that contains sufficient samples of 3D structures with all

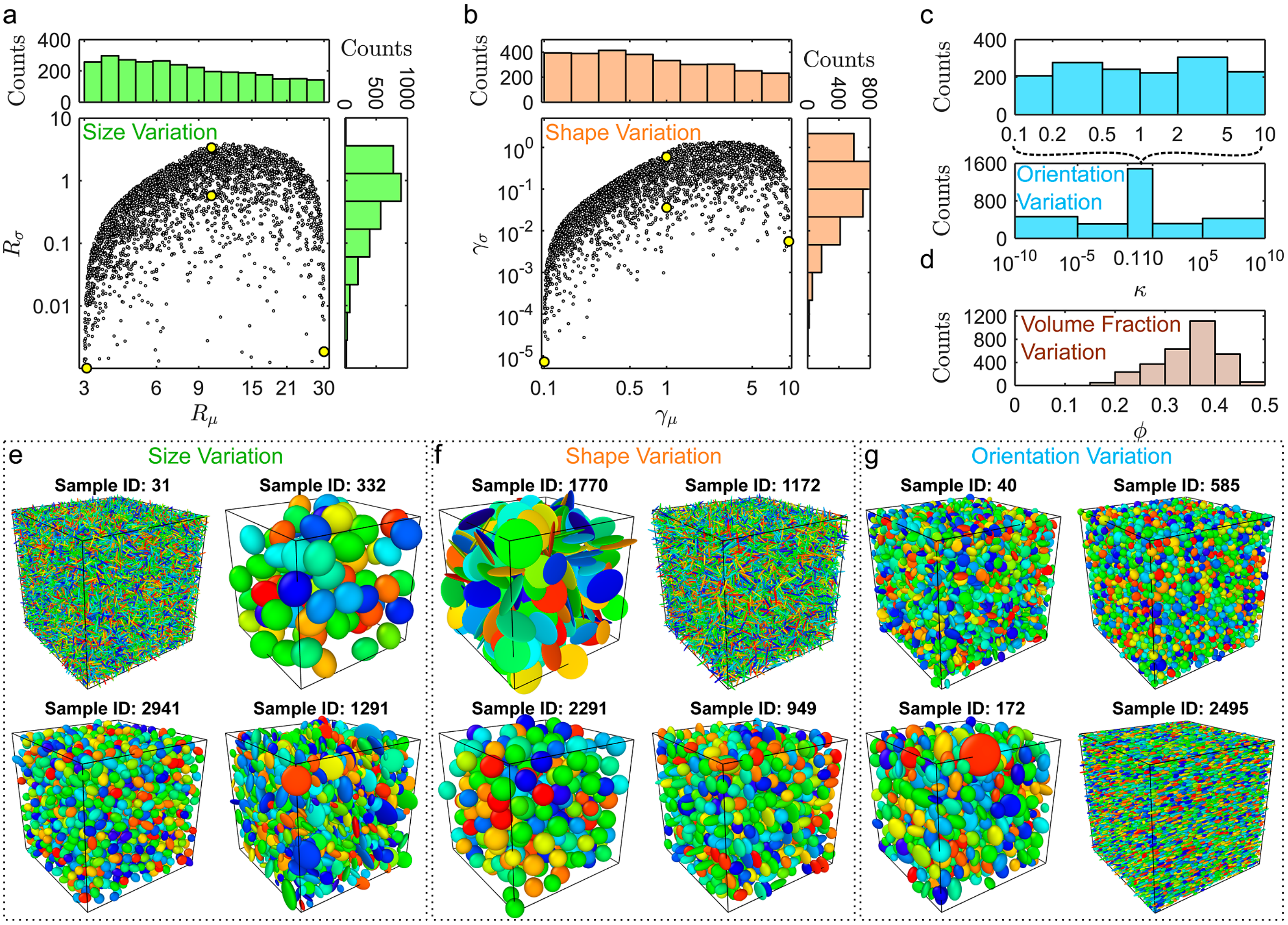

**Figure 2.** (a) Histograms and scatter plots describing how the mean and standard deviations of the volumetric radius $R$ are varied in each of the 3000 samples in the data set. (b) Similar to (a), but for the mean and standard deviations of the aspect ratio $\gamma$. (c) Histograms describing the distribution in the orientational anisotropy parameter $\kappa$ for the vMF distribution.[30] The histogram in the range of $0.1 \leq \kappa \leq 10$ is shown separately (on top) to indicate the distribution of nearly 50% samples uniformly drawn from this range. (d) Histogram describing the distribution in the volume fraction $\phi$ of the generated structures. (e−g) Representative snapshots of 3D structures drawn from the data set, showing size, shape, and orientation variations, respectively. The use of different colors facilitates easy distinction of individual particles visually. The structures in (e) and (f) correspond to points highlighted in the scatter plots of (a) and (b), respectively. The detailed information about their structural features is provided in Table 1.

potential variations in structural features that influence their computed 2D scattering profiles. This subsection describes this process of generating such a data set.

In principle, structural features condense the detailed representation (e.g., $x$, $y$, and $z$ coordinates of all particles) of the 3D structure to a few numerical values that pertain to the distributions of parameters describing the 3D structure. In the ML jargon, structural features are similar to the lower dimensional latent space variables encoding a higher-dimensional input function. Our philosophy is that the structural features should be information that a soft materials researcher would understand and find relevant. By relevance, we mean that the interested structural features (e.g., shapes, sizes, and spatial arrangement of the domains, extent of mixing/demixing within domains/between domains, orientational alignment of domains, grain boundaries, etc.) will likely control properties/function of the soft material. Thus, we choose not to have automatically encoded latent space variables that lack a physical meaning and are not easily interpreted by humans and instead, define our own structural features using our soft material domain knowledge.

To demonstrate our choices of structural features for a representative example of soft materials with structural anisotropy, we consider a model system of spheroidal particles with well-defined distributions of shapes, sizes, and orientations (shown schematically in Figure 1), along with variations in the particles' packing fractions in the material. Generation of such 3D structures is facilitated by our recently developed (open source) computational method called CASGAP (computational approach for structure generation of anisotropic particles).[30] In the original manuscript,[30] we demonstrated the versatility of the CASGAP method to generate 3D structures for user-provided distribution of particle sizes, shapes, and orientations at or close to the target volume fraction. Accordingly, the CASGAP method uses parameters $R_\mu$, $R_\sigma$, $\gamma_\mu$, $\gamma_\sigma$, and $\kappa$ to generate the 3D anisotropic structure with a target $\phi_{\text{target}}$. These structural descriptors serve as the structural features for use in this development of the CREASE-2D workflow. While the detailed description of these structural features can be found in the original manuscript,[30] we review some relevant details below:

**Table 1. Values of Structural Features for Selected Few Samples, in the Same Order as Shown in Figure 2**[a]

| Sample ID | $R_\mu$ | $R_\sigma$ | $\gamma_\mu$ | $\gamma_\sigma$ | $\kappa$ | $\phi$ |
|---|---|---|---|---|---|---|
| 31 | **3.07** | 0.00101 | 7.48 | 0.263 | $3.11 \times 10^{-1}$ | 0.245 |
| 332 | **30.0** | 0.00185 | 0.785 | 0.0352 | $4.41 \times 10^{-1}$ | 0.389 |
| 2941 | 10.2 | **0.576** | 1.28 | 0.200 | $5.89 \times 10^{-10}$ | 0.361 |
| 1291 | 10.2 | **3.38** | 0.488 | 0.176 | $6.31 \times 10^{0\circ}$ | 0.401 |
| 1770 | 17.4 | 1.87 | **0.100** | 0.000 | $2.18 \times 10^{-2}$ | 0.237 |
| 1172 | 3.57 | 0.201 | **9.96** | 0.00558 | $1.36 \times 10^{-1}$ | 0.194 |
| 2291 | 19.5 | 2.19 | 1.00 | **0.0358** | $1.35 \times 10^{8}$ | 0.422 |
| 949 | 12.9 | 0.802 | 1.00 | **0.591** | $3.83 \times 10^{4}$ | 0.409 |
| 40 | 7.80 | 1.50 | 0.511 | 0.0696 | $\mathbf{1.09{\times}10^{-10}}$ | 0.430 |
| 585 | 6.80 | 1.63 | 0.881 | 0.0669 | $\mathbf{1.23{\times}10^{-1}}$ | 0.461 |
| 172 | 14.1 | 3.69 | 0.654 | 0.122 | $\mathbf{9.70{\times}10^{0}}$ | 0.459 |
| 2495 | 3.64 | 0.0662 | 2.99 | 1.24 | $\mathbf{9.68{\times}10^{9}}$ | 0.357 |

[a] Bolded text is used to highlight the relevant structural features depicted in Figure 2.

1. The particle sizes and shapes are expressed by the spheroidal volumetric radius $R = \sqrt[3]{a^2c}$ and the spheroidal aspect ratio $\gamma = c/a$, where $a$ and $c$ are the lengths of the semiminor and semimajor axes of the spheroid, respectively. As done in the original manuscript,[30] the variations in the size and shape are modeled by a log–normal distribution, each with their means ($R_\mu$, $\gamma_\mu$) and standard deviations ($R_\sigma$, $\gamma_\sigma$). These quantities provide us with the first four structural features for CREASE-2D.
2. The orientation in the structure is quantified by a 3D vector pointing along the major axis $V$ of the spheroid. With such description of orientations, we adopt the 3D von Mises–Fisher (vMF) distribution (see details in ref 30) to model the distribution of the orientational order expressed succinctly by the $\kappa$ parameter. The $\kappa$ parameter is a measure of the inverse dispersity in orientation and is defined around a preferred orientation $\Lambda$. $\kappa = 0$ indicates complete lack of the orientational order (i.e., $V$ is uniformly distributed on the surface of a sphere) and $\kappa \to \infty$ indicates the perfect orientational order (i.e., $V = \Lambda$). Relying on the premise that for an anisotropic structure, the principal axes of anisotropy can be aligned with the laboratory frame of reference during scattering measurements such that $\Lambda = \hat{x}$, enables us to use only $\kappa$ as the fifth structural feature.
3. Lastly, the concentration of particles is quantified by the volume fraction of particles, $\phi$. If dense particle configuration is desired, a trade-off is observed between the computational time for structure generation and the value of volume fraction achieved in that time. The CASGAP method is designed with this trade-off in mind and can be terminated at any point of the structure generation while maintaining a structure that adheres to the desired structural features' distribution. However, in such cases of early termination, the actual volume fraction $\phi$ may not reach the value of $\phi_{\text{target}}$ leading to $\phi \le \phi_{\text{target}}$. With such an expectation, we use the actual $\phi$ evaluated after the structure is generated as the sixth structural feature since the scattering profile computed in step 2 (described in the next subsection) can be significantly influenced by the actual volume fraction of the particles.

Leveraging the computational efficiency of the CASGAP method, we generate a data set of 3000 3D structures. This data set has a numerical index from 1–3000 used as their Sample ID along with numerical values of all their structural features. We share some examples from this data set openly on Zenodo.[31] In Figure 2, we describe how each of the structural features are varied. Since each structural feature represents a physically relevant quantity with significant influence over the morphology of the particles, these could not simply be varied using a uniform distribution over their respective ranges. As a result, some of these quantities have a normal-like or a skewed distribution in their chosen ranges, as shown in the plots in Figure 2a–d. The numerical details of the random sampling, which is a version of the Monte Carlo sampling, are discussed in detail in Supporting Information Section S1. We represent all our structures by a cubic representative volume of length $L = 300$ distance units (in this study, 1 distance unit corresponds to 1 Å, but this correspondence can be changed to a different length scale, as desired). Figure 2e–g and the accompanying Table 1 provide some representative structure snapshots along with their structural features. Some extreme values of structural features have been listed in Table 1 with bold font; we selected the Sample IDs with these extreme values of structural features to visualize their effects on the overall structure.

The mean volumetric radius ,$R_\mu$, is nearly uniformly sampled over a range of 3 to 30 Å, representing a variation of 1% $L$ to 10% $L$ (as shown in the histogram of Figure 2a). To keep the size variation reasonable within the prescribed log–normal distributions, the standard deviation of volumetric radius is controlled by the mean value, such that whenever $R_\mu$ approaches its extreme values, i.e., 3 or 30 Å, $R_\sigma \to 0$. This is shown in the scatter plot of Figure 2a, where an envelope shape over the $R_\sigma$ distribution is observed. In Figure 2e, sample 31 and sample 332 depict the structure when $R_\mu$'s are ~3 and ~30, respectively. While Sample IDs 2941 and 1291 (with similar $R_\mu$) depict the extreme values of $R_\sigma$.

Figure 2b shows the variation in aspect ratio, $\gamma$, in the range of 1/10 to 10. Since this is a ratio, the values below 1 (representing oblate spheroids) are analogous, by a reciprocal relationship, to those above 1 (representing prolate spheroids). To ensure fair sampling of both of these shape types, the values are nearly uniformly sampled over the logarithmic scale between 1/10 and 10, as shown in the histogram of Figure 2b. Here, too, we ensure that whenever the mean aspect ratio $\gamma_\mu$ approaches the extremes, $\gamma_\sigma$ approaches 0 as seen from the scatter plot in Figure 2b. In Figure 2e, Sample IDs 1770 and 1172 depict the structure when $\gamma_\mu$'s are ~0.1 and ~10, respectively. While Sample IDs 2291 and 949 (with similar $\gamma_\mu$) depict extreme values of $\gamma_\sigma$.

To vary the degree of the orientational order, the $\kappa$ parameter (Figure 2c) can be varied by sampling equally from four intervals defined by the end points: $10^{-10}$, 0.1, 1, 10, and $10^{10}$. Here, values $10^{-10} \approx 0$ and $10^{10} \approx \infty$ are chosen to sample the perfectly isotropic and anisotropic structures, respectively. Structures from each of these intervals are in Figure 2e with Sample IDs 40, 585, 172, and 2495, where $\kappa$ values are nearly $10^{-10}$, 0.1, 10, and $10^{10}$, respectively.

In Figure 2d, the histogram shows the variation in volume fraction, $\phi$, for the entire data set. Unlike all other structural features, the distribution of volume fraction $\phi$ is not prescribed but is a result of CASGAP structure generation with $\phi_{\text{target}}$ = 0.5, as explained previously. If a stricter control over $\phi$ is desired, more samples at lower $\phi$ can easily be generated and added to the data set to change the shape of the distribution.

Having the data set of 3D structures, we calculate each of their 2D scattering profiles in step 2. The 2D scattering profiles and the structural features then become the intended "output" and "input" data for training and testing the surrogate ML model in step 3, respectively.

### Step 2: Calculating 2D Scattering Profile for Each 3D Structure

In all previous implementations of the CREASE method, we used the pairwise Debye scattering equation to calculate the scattering intensity contribution of $N$ particles with known form factors $f_{1,2,...,N}(q)$ as follows

$$I_{\text{comp}}(q) = \frac{1}{V} \sum_{n=1}^{N} \sum_{m=1}^{N} f_n(q) f_m(q) \frac{\sin(q r_{nm})}{q r_{nm}} \tag{1}$$

The above equation is only applicable for isotropic arrangement of particles and is obtained by integration over all possible orientations of the scattering vector $\mathbf{q}$, which is equivalent to azimuthal averaging performed on the experimental 2D scattering profiles. Notably, this equation has a double-summation term which necessitates pairwise consideration of particles and their contributions to the scattering profiles and has the effect of making the scattering calculations computationally intensive and harder to parallelize. Together with the time required to generate structures, the additional time needed to perform scattering calculations for that structure makes them unfit for use directly within the CREASE workflow. This motivated the need for surrogate ML models that are time efficient in the prediction of $I_{\text{comp}}(q)$ (as described in step 3 subsection).

For CREASE-2D implementation, we compute the 2D scattering intensity $I_{\text{comp}}(\mathbf{q})$ from the scattering amplitude $A_{\text{comp}}(\mathbf{q})$ as $I_{\text{comp}}(q) = 1/V|A_{\text{comp}}(\mathbf{q})|^2$. Here, the $A_{\text{comp}}(\mathbf{q})$ is the complex Fourier transform of the fluctuation in the scattering length density $\Delta\rho_n$,[32−34] and is expressed as

$$A_{\text{comp}}(\mathbf{q}) = \sum_{n=1}^{N} \Delta\rho_n v_n f_n(\mathbf{q}) \exp(-i\mathbf{q}\cdot\mathbf{r}_n) \tag{2}$$

The above expression only has a single summation term, which significantly reduces the computational complexity of the scattering calculation from $O(N^2)$ to $O(N)$ and has enabled the computation to be parallelized; this was also noted by Brisard and Levitz as the "simple sums" computation.[34] For our model system, due to the simplicity of the ellipsoidal shape, computation of eq 2 is further simplified with the anisotropic form factor $f_n(\mathbf{q})$ of a spheroid, which can also be obtained from Pedersen's tabulation of analytical form factors.[8] $f_n(\mathbf{q})$ is provided as

$$f_n(\mathbf{q}) \equiv f_n(q, \theta) = \frac{j_1(q r_n(\theta))}{q r_n(\theta)} \tag{3}$$

In the above equation, $j_1(\cdot)$ is the first spherical Bessel function, and $r_n(\theta)$ is an effective radius (of particle $n$) that depends on the azimuthal angle $\theta$. A more detailed expression for the analytical form factor can be found in Supporting Information Section S2. We note that for shapes of particles that are complex, without easily available analytical forms of shapes, one can calculate the entire 2D scattering profile by placing point scatterers in the box and using a sufficient number of point scatterers to resolve the particle shapes and particle−particle spatial arrangements. We are currently finalizing a computational efficient, GPU-based code, to calculate 2D scattering profiles for any shape of the particle using this scatterer approach; we will share that as open-source code on https://github.com/arthijayaraman-lab.

As the structure is contained in the shape of a cubical box of length $L$, the scattering calculations can be heavily dominated by the form factor of the cubical box, referred to as the "finite size effects" in the literature.[34] These finite size effects greatly obscure the 2D scattering profile of the structure and make it hard to interpret their variation purely due to the structural features. By accounting for the volume fraction of each particle, we can subtract the form factor of the box as a correction to the scattering profile of the structure. We have adapted the correction scheme described by Brisard and Levitz[34] to remove these finite size effects as discussed in Supporting Information Section S2. Some simplifications such as considering the full shape of the particles at the boundaries can be made and work well as long as the cubic box size is much larger than the size of the particles, which in our case is below 10% $L$.

We note that in real experimental measurements, the scattering profiles are sometimes influenced heavily by noise, positions of the beam stops, the choice of the $q$-ranges, and/or other factors like Ewald sphere curvature-related distortions. All of these factors may affect the correct interpretation of the scattering data. If these effects on experimental scattering profiles cannot be removed successfully prior to analysis by CREASE-2D, then we can emulate them and incorporate them in the computed scattering profiles in step 2. Subsequently, the surrogate ML model can be trained on these more "realistic" scattering profiles.

Figure 3a−f provides some representative examples of scattering profile variations computed using eq 3 after applying the finite size effects correction. In each panel, a structure denoted by their Sample ID is shown together with two representations of the computed scattering profiles, which are obtained as the color-coded intensity plots for each $q$ and $\theta$ value. The left scattering plots in Figure 3 are referred to as the Cartesian scattering intensity plots, $I_{\text{comp}}(q, \theta)$, with axes magnitude of scattered wave vector $q$ and azimuthal angle $\theta$. The right scattering plots show the polar form of the scattering plot: scattering intensity $I_{\text{comp}}(q_x, q_y)$, with axes $q_x$ and $q_y$, two components of scattering vector $\mathbf{q}$. The polar form is easily recognizable to the soft materials experts, and is the typical representation of 2D scattering profiles directly produced from SAXS/SANS measurements. Both the "Cartesian" and "polar"

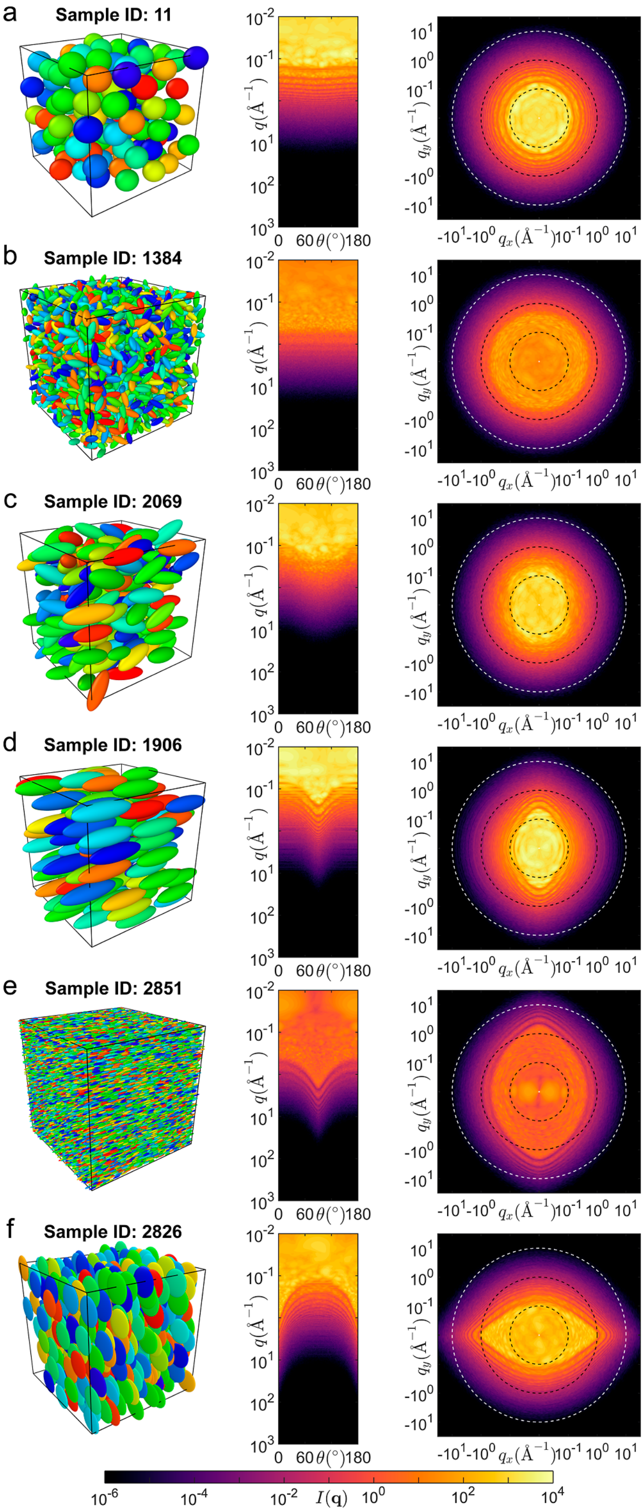

**Figure 3.** (a−f) From left to right, representative snapshots of a structure with Sample ID denoted on the top, the Cartesian form of their scattering intensity profile $I_{\text{comp}}(q, \theta)$ with axes magnitude of scattered wave vector $q$ and azimuthal angle $\theta$, and the polar form of their scattering intensity profile $I_{\text{comp}}(q_x, q_y)$ with axes $q_x$ and $q_y$. Here, $q_x$ and $q_y$ are components of the scattering vector $\mathbf{q}$ that are (reciprocally) aligned with the laboratory frame axes $x$ and $y$, respectively. The polar form of the scattering intensity profile maintains the logarithmic scaling of the scattering vector magnitudes, and as a result the center of the profile is not at $q = 0$ but truncated to $q = 10^{-2}$.

forms of 2D scattering profiles are numerically equivalent and only differ in their visual representation. We have included the polar scattering intensity plots as a reference to the reader for easier comparison to relevant experimental scattering profiles. However, for the further analysis, the Cartesian representation provides a convenient and straightforward representation of the numerical data, since only half of the complete plot $\theta = 0°$ to $\theta = 180°$ needs to be represented due to the inversion symmetry with the other half of the profile, i.e. $I(\mathbf{q}) = I(-\mathbf{q})$. As demonstrated further, the Cartesian representation can be easily serialized to obtain the complete training and testing data in a tabular form that is convenient for training the surrogate ML model as described in the next subsection.

The structures chosen in Figure 3 are used to demonstrate how structural variations can influence the scattering profile. For example, Figure 3a,b each demonstrate an isotropic scattering profile, while having different shapes of the individual particles; more spherical in the former and disordered (low $\kappa$) prolate-spheroidal in the latter. Figure 3c shows weakly aligned structure (intermediate $\kappa$), while Figure 3d−f show highly aligned structures (high $\kappa$). Another distinguishing effect is the change in the intensity at low $q$ for Figure 3d,e; this is due to the drastic change in the average size of the particles. One can see similarities between the qualitative trends of increasing local alignment in structural configurations, and the tightening of the scattering profile along the axial direction, with the observations for semiflexible polymer systems as they undergo isotropic to nematic transition as depicted in refs 35 and 36.

### Step 3: Training the ML Model to Link Structural Features to Computed Scattering Profiles

With a streamlined implementation of steps 1 and 2, the data set of 3000 3D structures and their corresponding 2D scattering profiles is ready for the ML model training and testing (or validation). 80% of the data (2400 structures) is used for training the ML model and the remaining 20% (600 structures) is used for validation of the ML model's performance.

In our efforts to apply an appropriate ML method that predicts the 2D scattering profile from a given set of structural features, we identify the need to use a supervised ML approach, where continuous-valued quantities can be predicted from a small set of other continuous parameters. Traditionally, both deep learning (DL) and ensemble learning approaches have been successfully applied to achieve these tasks.

With the many DL approaches, one can create a generative model that is conditionally trained on all of the structural features. However, successful training of generative models requires a lot more data than provided in our data set, roughly estimated to be well above 10,000−100,000 images for model training alone.[37,38] On the other hand, ensemble learning methods combine the prediction of multiple standalone models, to create an overall "ensemble" predictive model that is more accurate than the individual predictions from the standalone models. Many ensemble learning approaches can be easily implemented using decision trees, which are simpler to work with than neural networks, and have been shown to perform exceptionally well, outperforming neural networks[39] for tabular data, as is also the case for $I_{\text{comp}}(q, \theta)$. Motivated by these advantages, we use a decision tree-based ML model to predict the value of $I_{\text{comp}}(q, \theta)$ for each of the 6 structural features and the given $q$ and azimuthal angle $\theta$ values.

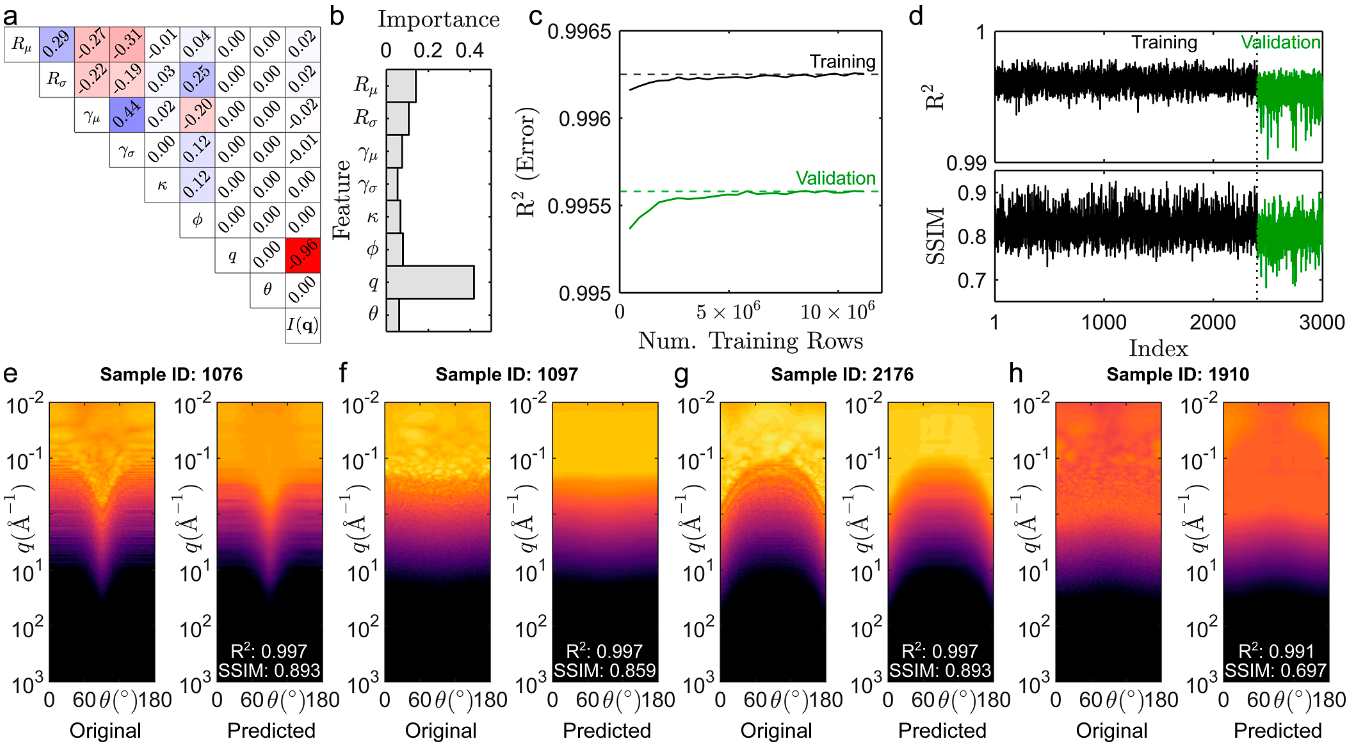

**Figure 4.** (a) Correlation matrix for all 6 structural features along with $q$, azimuthal angle $\theta$ and $I(\mathbf{q})$ values that together form the data set for training and validation. (b) Importance histogram for each feature evaluated by the model after training. (c) Learning curve during training of the surrogate ML model, where $R^2$ error of the training (black) and validation (green) data entries is plotted against the number of data entries. (d) Performance of the ML model using the $R^2$ and the structural similarity index measure (SSIM) scores for all 3000 samples in the data set. We note that the index in the $x$-axis for this plot runs from 1 to 3000 but it is different from Sample IDs; the index distinguishes the randomly selected 2400 samples used for training and 600 samples for the validation. (e−h) Original and predicted scattering profiles for a selected few samples from the validation data set, each marked with their $R^2$ and SSIM scores.

In the realm of decision tree-based ML models, especially when dealing with tabular data, boosting ML techniques have gained popularity.[40−43] This is because boosting ML techniques combine groups of weak predictive learners sequentially and correct previous models' training loss to form a strong ensemble model. Here, we choose the XGBoost algorithm,[44] which stands for eXtreme Gradient Boosting, to be the surrogate ML model in CREASE-2D, due to its exceptional performance and lower scope of overfitting.

XGBoost is a generalized algorithm that can be implemented to solve a wide range of problems. During training, XGBoost assigns weights to all features it trains on, referred to as feature importance, and accordingly adjusts the construction of decision trees. XGBoost also offers a wide range of hyper-parameters that can be fine-tuned to a diverse set of training data. In our work, we utilize these advantages of XGBoost to train the surrogate ML model that outputs a 2D scattering intensity for the input of structural features and $(q, \theta)$ values.

To use the XGBoost algorithm, the training data set is reformatted into a table, where each row contains all 6 structural features as fields, combined with a serialized representation of the scattering profiles. Thus, each training data set row reads as $R_\mu$, $R_\sigma$, $\gamma_\mu$, $\gamma_\sigma$, $\kappa$, $\phi$, $q$, $\theta$, and $I(q, \theta)$. During serialization of the data set, the resolution of the scattering profile can have a dominant effect on the efficiency of training. This is because a higher resolution will result in better quality of the data but also increases the computational overhead and memory requirements during training. The 2D scattering profiles calculated in step 2 are generated over a $(q, \theta)$ grid of 501 × 181 = 90,681 data points, which amounts to over 200 million points for all 2400 samples in the training data set. In principle, one could use all these points to train the surrogate ML model, if the user has outstanding computational resources with limitless memory. For users with modest computational resources (including cost-effective subscriptions to Google Colab), subsampling of the data is deemed necessary. We therefore adopted a grid-based subsampling approach where we uniformly sample every fourth $q$ value and every fifth $\theta$ value to obtain a $(q, \theta)$ grid of 127 × 37 = 4662 data points. This results in around 11 million tabular entries for the 2400 samples that can be handled reasonably well by the ML model.

To tune the architecture of the decision trees in the XGBoost model, Bayesian search optimization[45] with cross-validation is performed over a large range of hyperparameters to identify their best configuration that provides reliable accuracy in the predicted 2D scattering profiles. More details about configurations of Bayesian optimization are provided in Supporting Information Section S3. As an example, after this optimization, we find that the predicted intensity values are the most reliable when for each decision tree and for each node of a decision tree, only 90 and 80% of the structural features are randomly sampled, respectively. Other hyperparameters that determine the learning rate, step size, maximum depth of the decision tree, etc., are also optimized and described in more detail in Supporting Information Section S3 along with their optimum values that are used to train the ML model. Careful tuning of these hyperparameters is essential for achieving optimal model performance and avoiding overfitting on the given data set. Bayesian optimization of the hyperparameters takes just over an hour to optimize, when using the V100 GPUs with 51 GB RAM as provided by our Google Colab Pro subscription. Once the tuned hyperparameters are obtained, the XGBoost model is trained on CPUs within 10 min.

To understand the data, we present the correlation matrix in Figure 4a and to understand how the ML model interprets the data after training, we present the histogram that measures the feature importance in Figure 4b. The correlation matrix indicates weak correlations between the means and standard deviations of $R$ and $\gamma$, possibly due to the way these values are sampled, as indicated in step 1. Some correlations are also observed for volume fraction $\phi$ and all remaining structural features; as noted above in the CASGAP structure generation, the volume fraction $\phi$ value is not directly varied during structure generation and is evaluated only after the structure is generated. The strongest (inverse) correlation is observed between the scattering intensity $I(q, \theta)$ and the magnitude of the wavevector $q$; this is expected as the scattering intensity values display a drastic dependence on the $q$ values. Consequently, after training, the ML model assigns the highest importance to $q$, as shown in Figure 4b. Figure 4c shows the learning curve where the performance is measured using the $R^2$ error, which is a normalized version of the mean squared error (MSE) and plotted against the number of data entries that the model has already used for training. Both training and the validation errors are found to converge quickly to beyond 99.5%, indicating that the surrogate ML model does not over fit the training data.

In Figure 4d, we evaluate the performance of the surrogate ML model using two metrics for all 3000 samples, where we have assigned an index (different from Sample ID) to separate the training samples from the validation (or test) samples. The first metric is the $R^2$ error evaluated in a similar way as done during ML model training. These $R^2$ scores provide information about the prediction accuracy of the ML model at each $q$ and $\theta$ value on an individual basis (i.e., without necessarily considering the local context). We find that the $R^2$ values converge to 0.995 and do not differ much for training vs validation samples, indicating excellent prediction accuracy of the ML model. However, to also evaluate the performance of the ML model to output the entire 2D scattering profile, we need another metric that takes into account the performance of the model at all values in the local vicinity of $q$ and $\theta$. For this reason, we choose the structural similarity index measure (SSIM) score which infers the structural differences between the two scattering profiles, by using image-based characteristics like luminescence, contrast, and pattern; these quantities are derived from the mean, variance, and covariance information on the local pixel data. An SSIM score near 1 indicates a good performance of the ML model in predicting the entire scattering profile for a given set of structural features. In Figure 4d, the SSIM scores converge to above ~0.8, indicating a reliable prediction accuracy of the ML model.

A visual comparison between the original and the ML-predicted scattering profiles is also shown in Figure 4e−h, along with their $R^2$ and SSIM scores. We note that among all of the Sample IDs, Sample ID 1910 shown in this figure has the least SSIM score. A more detailed comparison between the original and predicted profiles is provided in Supporting Information Section S4, by overlaying their 1D scattering profiles at a few selected $\theta$ values to further demonstrate the similarities in the two profiles. These results demonstrate that the trained surrogate ML model performs reasonably well. It is important to note that the quality of the surrogate model training will impact how well CREASE-2D performs. We encourage the users of CREASE-2D to invest the appropriate time for the ML model training and to ensure that poor training and testing do not manifest as poor analyses from CREASE-2D.

## Step 4: Optimization within GA in CREASE-2D

The final step in the CREASE-2D implementation is to put together the predictive capacity and the speed of the surrogate ML model within the GA optimization loop. We refer the reader to previous CREASE publications[18−26] for detailed implementations of the GA optimization loop in the successful execution of the CREASE (1D) method. In the current implementation, one major distinction is the use of a continuous parameter GA in contrast to the binary GA used in the previous work. The continuous parameter GA is better suited for evolving "genes" that represent continuous parameters, and has a more straightforward interpretation of the crossover and mutation operations.[46] As noted before, the 6 structural features ($R_\mu$, $R_\sigma$, $\gamma_\mu$, $\gamma_\sigma$, $\kappa$, $\phi$) are represented as 6 corresponding "genes" and every "individual" has a unique set of values for these genes in the GA optimization loop. We first normalize values of the genes, using a scheme similar to the one used to obtain their randomized distribution; for more detail see Supporting Information Section S5. The normalization schemes assign a value between 0 and 1 as the value of the gene and have a monotonic one-to-one correspondence with the value of the corresponding structural feature.

For every "individual" with a unique set of genes, a scattering profile is predicted from the surrogate ML model using the individual's structural features as the input. All individuals in each generation are then ranked by their "fitness" value which is quantified by the SSIM of the individual's computed scattering profile with respect to the experimental input scattering profile. The objective of the GA optimization loop is to improve the fitness of an individual; in other words, improvement of the SSIM score of its computed scattering profile $I_{\text{comp}}(q, \theta)$ as compared to $I_{\text{exp}}(q, \theta)$.

The other important consideration in the implementation of the GA optimization loop is the choice of the number of individuals to sample in each generation (i.e., the population size) as well as the selection procedures for determining individuals that move to the next generation. In our implementation, we use a fixed population of 100 individuals per generation that is always ranked according to their fitness. In each generation, the top 30 individuals with the highest fitness are selected. These 30 individuals serve as parents who are randomly paired to form 70 children using a single-point crossover method. Subsequently, the 30 parents and 70 children together form 100 individuals for the next generation. For these 100 individuals, the next set of operations is related to mutation. The top two elite individuals' gene values are kept unchanged as they progress to the next generation. The remaining 98 individuals undergo adaptive mutation, where the mutation probability and step size are varied based on the L2 distance (or the squared Euclidean distance) of the individual from the mean value of all individuals. Adaptive mutation is usually recommended to prevent the GA from converging too quickly to a local minimum and to have sufficient diversity in the genes and individuals in the

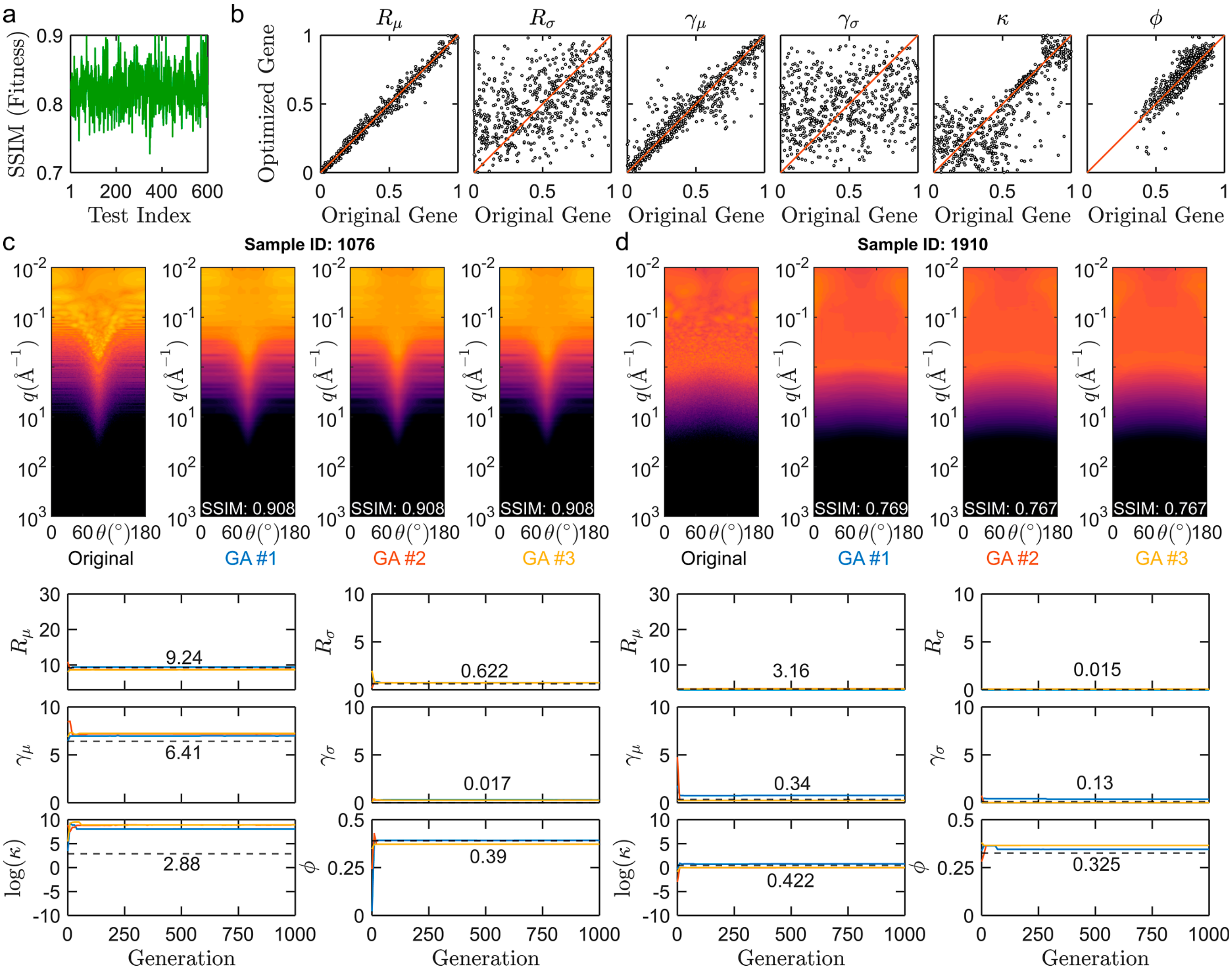

**Figure 5.** Performance of GA in CREASE-2D. (a) SSIM scores for all 600 test samples as input to CREASE-2D; SSIM quantifies the similarity between the GA-optimized or "best" $I_{\text{comp}}(q, \theta)$ at the end of the GA loop with the input $I_{\text{exp}}(q, \theta)$. (b) The comparison of GA-optimized values of the normalized "gene" or structural features and the original value of the structural feature, normalized to represent a target gene value for all 600 samples tested with CREASE-2D. (c,d) Two selected samples—Sample IDs 1076 and 1910—out of the 600 samples tested with CREASE-2D. We show visual comparison of the input scattering profile and outputs from three independent GA runs and plot their corresponding evolution of structural feature predictions during each GA run for Sample IDs 1076 and 1910. The solid colored curves in the plots in (c,d) are the three GA runs and the black dashed curve is the value of the structural feature corresponding to the original scattering, with the exact value of that structural feature denoted in the text.

population.[47] With this next generation of 100 individuals, the GA optimization loop is then continued. As the number of generations increases, the fitness of a generation should converge, and upon convergence, the GA loop can be stopped.

## PERFORMANCE OF CREASE-2D

To evaluate the performance of the CREASE-2D method, we use all 600 test samples out of the 3000 total samples (the reader will recall that out of the data set of 3000 samples, 2400 samples are used to train the surrogate model) and run GA five separate times for each sample. We run five GA separate runs for each sample to check how different the output structural features from CREASE-2D are for each sample's input scattering profile; this allows us to understand degeneracy in optimized GA solutions. In Figure 5a, the fitness measured in the form of the SSIM scores for all 600 samples, tested in CREASE-2D, are all found to be in the 0.7 to 0.9 range. We note that this SSIM score range is similar to the performance of the surrogate ML model indicating a reliable match between the input and output scattering profiles. For each sample, the standard deviations in the SSIM scores from its five GA replicates are small (within 1% of the value shown) and thus, not shown in the plot for clarity. We note that CREASE-2D method performs only as well as the surrogate ML model and it should not be expected to outperform the prediction accuracy of the surrogate ML model.

In Figure 5b, we compare how well CREASE-2D predicts each structural parameter value for all 600 test samples whose structural features we (but not CREASE-2D) know a priori. To make an effective visual comparison, we use the gene values directly instead of the structural features in these plots. For some structural features, especially $\phi$, $R_\mu$, and $\gamma_\mu$ (i.e., volume fraction and means of particle size and shape distributions), the accuracy of prediction is high, as indicated by the clustering of points close to the red line with the unit slope. For $R_\sigma$ and $\gamma_\sigma$ (which measure the dispersity in the particle size and shape), the prediction accuracy is low, despite having a high SSIM score. This indicates that precise values of the extent of dispersity in the particle size and shape have a minimal impact on the variation of the scattering intensity; this is in line with observations in experiments that the presence of dispersity broadens peaks of the scattering profile but does not alter the shape of the profile with the value of dispersity. As a result, for $R_\sigma$ and $\gamma_\sigma$, the CREASE-2D method is dealing with larger degeneracy in solutions. For $\kappa$ that quantifies the orientational order, the accuracy is high only for samples that have high values of $\kappa$, and the accuracy is low for samples with lower $\kappa$ values (i.e., low orientational order). As one would expect, at low values of $\kappa$ which represent isotropic ordering of anisotropic particles, the precise numerical value of the $\kappa$ value has minimal impact on the scattering intensities.

To further demonstrate the performance of the CREASE-2D method for the four representative samples (same as from Figure 4), in Figure 5c,d, the results for Sample IDs 1076 and 1910 are presented, and the results for Sample IDs 1097 and 2176 are provided in Supporting Information Section S5. The evolution of their fitness values is also presented in Supporting Information Section S5. In Figure 5, we show the predicted scattering profiles for the best outputs from 3 out of the 5 GA runs per system along with the evolution of structural features over 1000 generations from those 3 GA runs. In each run, the GA loop converges closely to the original value of the structural feature in the first few generations, as indicated by the convergence of the curves to the dashed line (the numbers in the plots denote the target structural feature value of that sample). We note that one GA optimization loop with 1000 generations of 100 individuals uses 30−45 min in real time to complete when implemented on a single-(CPU) core laptop/computer with modest hardware.

We would like to emphasize that our choice of the model system with spheroidal particles and the variation of relevant structural features was motivated by the convenience of generating structures using the existing CASGAP method.[30] To extend CREASE-2D to interpret 2D scattering profiles from other soft material systems (e.g., processed polymers with orientational alignment or structures accessed during rheology in Rheo-SANS experiments), the user should follow similar steps as described for the model system: (1) identify the structural features of relevance (e.g., orientational order parameters, and distribution of domain sizes and shapes); (2) generate "synthetic" or in silico structures for varying values of such structural features; (3) calculate the 2D scattering profiles using the scatterer placements within these structures; (4) train the surrogate XGBoost model or other ML models with such structures as input and 2D scattering profiles as output; and (5) incorporate the surrogate model within the CREASE-2D loop to optimize toward the structural features that gives rise to a scattering profile like the input scattering profile.

In conclusion, we have developed a new CREASE-2D method that analyzes 2D scattering profiles as is without any averaging along all or few angle- and output-relevant structural features like domain size and shape distribution, extent of the orientational order in the structure, and packing fraction of the domains in the structure. The development of CREASE-2D relied on the generation of the data set with 3000 samples each with a desired set of structural features and the corresponding 3D structures generated using CASGAP[30] and the corresponding computed 2D scattering profile. This data set enabled training of a surrogate XGBoost-based model that outputs the 2D scattering profile for a given set of structural features. Using this surrogate ML model within a GA optimization loop, we are able to identify all of the structural features (and reconstruct 3D real-space configurations, if needed) that produce a scattering profile that matches the input 2D scattering profile. We believe that soft material researchers who aim to understand how macroscopic properties (e.g., rheology and flow) depend on the structural anisotropy and the hierarchy of structural length scales within the materials will find this CREASE-2D method useful. CREASE-2D enables users to analyze the output of scattering experiments holistically without having to use approximate analytical models to fit to averaged 1D profiles or limit analysis to only averaged angular sections of the 2D profiles.

## ■ ASSOCIATED CONTENT

### Data Availability Statement

The open-source code for CREASE-2D is available on https://github.com/arthijayaraman-lab. The data set discussed in the paper is available on https://zenodo.org/records/10534943. The open-source code for the 3D structure generation method, CASGAP, is also available on https://github.com/arthijayaraman-lab.

### Supporting Information

The Supporting Information is available free of charge at https://pubs.acs.org/doi/10.1021/jacsau.4c00068.

Additional views of results presented in the main paper, and specific details about some of the steps in the method development (PDF)

## ■ AUTHOR INFORMATION

### Corresponding Author

**Arthi Jayaraman** − *Department of Chemical and Biomolecular Engineering and Department of Materials Science and Engineering, University of Delaware, Newark, Delaware 19716, United States;* orcid.org/0000-0002-5295-4581; Email: arthij@udel.edu

### Authors

**Sri Vishnuvardhan Reddy Akepati** − *Data Science Program, University of Delaware, Newark, Delaware 19716, United States*

**Nitant Gupta** − *Department of Chemical and Biomolecular Engineering, University of Delaware, Newark, Delaware 19716, United States;* orcid.org/0000-0002-3770-5587

Complete contact information is available at: https://pubs.acs.org/10.1021/jacsau.4c00068

### Author Contributions

$^\perp$S.V.R.A. and N.G. contributed equally to this work. A.J., S.V.R.A., and N.G. developed the ideas for this CREASE-2D method. A.J. received funding to support this project. N.G. and S.V.R.A. generated the data set of structures and scattering profiles. S.V.R.A. developed the surrogate XGBoost ML model to train on the data set and tested the model. N.G. and S.V.R.A. created the CREASE-2D workflow and implemented the genetic algorithm optimization. A.J., N.G., and S.V.R.A. wrote and edited the manuscript. CRediT: **Sri Vishnuvardhan R. Akepati** data curation, formal analysis, investigation, methodology, validation, visualization, writing-original draft, writing-review & editing; **Nitant Gupta** data curation, formal analysis, investigation, methodology, validation, visualization, writing-original draft, writing-review & editing; **Arthi Jayaraman** conceptualization, funding acquisition, project administration, resources, supervision, visualization, writing-original draft, writing-review & editing.

### Notes

The authors declare no competing financial interest.

## ACKNOWLEDGMENTS

We are grateful for financial support from the National Science Foundation (NSF, grant no. 2105744 for S.V.R.A. and A.J.) and MURI AFOSR (grant no. MURI-FA 9550-18-1-0142 for N.G. and A.J.) to complete this method-development work. We also acknowledge the use of DARWIN computing system for some of the computing in this work: DARWIN—A Resource for Computational and Data-Intensive Research at the University of Delaware and in the Delaware Region, which is supported by the NSF under grant no. 1919839, Rudolf Eigenmann, Benjamin E. Bagozzi, Arthi Jayaraman, William Totten, and Cathy H. Wu, University of Delaware, 2021.

## REFERENCES

(1) Wei, Y.; Hore, M. J. A. Characterizing polymer structure with small-angle neutron scattering: A tutorial. *J. Appl. Phys.* **2021**, *129*, 171101.

(2) Gräwert, T. W.; Svergun, D. I. Structural modeling using solution small-angle x-ray scattering (saxs). *J. Mol. Biol.* **2020**, *432*, 3078−3092.

(3) Jeffries, C. M.; Ilavsky, J.; Martel, A.; Hinrichs, S.; Meyer, A.; Pedersen, J. S.; Sokolova, A. V.; Svergun, D. I. Small-angle x-ray and neutron scattering. *Nat Rev Methods Primers* **2021**, *1*, 70.

(4) Lombardo, D.; Calandra, P.; Kiselev, M. A. Structural characterization of biomaterials by means of small angle x-rays and neutron scattering (saxs and sans), and light scattering experiments. *Molecules* **2020**, *25*, 5624.

(5) Semeraro, E. F.; Marx, L.; Frewein, M. P.; Pabst, G. Increasing complexity in small-angle x-ray and neutron scattering experiments: from biological membrane mimics to live cells. *Soft Matter* **2021**, *17*, 222−232.

(6) Breßler, I.; Kohlbrecher, J.; Thünemann, A. F. Sasfit: a tool for small-angle scattering data analysis using a library of analytical expressions. *J. Appl. Crystallogr.* **2015**, *48*, 1587−1598.

(7) Doucet, M.; Cho, J. H.; Alina, G.; Bakker, J.; Bouwman, W.; Butler, P.; Campbell, K.; Gonzales, M.; Heenan, R.; Jackson, A.; et al. *Sasview Version 4.1*; Zenodo, 2017. http://www.sasview.org.

(8) Pedersen, J. S. Analysis of small-angle scattering data from colloids and polymer solutions: modeling and least-squares fitting. *Adv. Colloid Interface Sci.* **1997**, *70*, 171−210.

(9) Pokorski, J. K.; Hore, M. J. Structural characterization of protein−polymer conjugates for biomedical applications with small-angle scattering. *Curr. Opin. Colloid Interface Sci.* **2019**, *42*, 157−168.

(10) Hammouda, B. *Probing Nanoscale Structures-The Sans Toolbox*; National Institute of Standards and Technology, 2008; Vol. *1*.

(11) Eberle, A. P.; Porcar, L. Flow-sans and rheo-sans applied to soft matter. *Cur. Opin. Colloid Interf. Sci.* **2012**, *17*, 33−43.

(12) Gordon, M. B.; Kloxin, C. J.; Wagner, N. J. Structural and rheological aging in model attraction-driven glasses by rheo-sans. *Soft Matter* **2021**, *17*, 924−935.

(13) Richards, J. J.; Wagner, N. J.; Butler, P. D. A strain-controlled rheosans instrument for the measurement of the microstructural, electrical, and mechanical properties of soft materials. *Rev. Sci. Instrum.* **2017**, *88*, 105115.

(14) Anker, A. S.; Butler, K. T.; Selvan, R.; Jensen, K. M. Ø. Machine learning for analysis of experimental scattering and spectroscopy data in materials chemistry. *Chem. Sci.* **2023**, *14*, 14003−14019.

(15) Friesner, R. A.; Abel, R.; Goldfeld, D. A.; Miller, E. B.; Murrett, C. S. Computational methods for high resolution prediction and refinement of protein structures. *Curr. Opin. Struct. Biol.* **2013**, *23*, 177−184.

(16) Dorn, M.; e Silva, M. B.; Buriol, L. S.; Lamb, L. C. Three-dimensional protein structure prediction: Methods and computational strategies. *Comput. Biol. Chem.* **2014**, *53*, 251−276.

(17) Franke, D.; Jeffries, C. M.; Svergun, D. I. Machine learning methods for x-ray scattering data analysis from biomacromolecular solutions. *Biophys. J.* **2018**, *114*, 2485−2492.

(18) Beltran-Villegas, D. J.; Wessels, M. G.; Lee, J. Y.; Song, Y.; Wooley, K. L.; Pochan, D. J.; Jayaraman, A. Computational reverse-engineering analysis for scattering experiments on amphiphilic block polymer solutions. *J. Am. Chem. Soc.* **2019**, *141*, 14916−14930.

(19) Heil, C. M.; Ma, Y.; Bharti, B.; Jayaraman, A. Computational reverse-engineering analysis for scattering experiments for form factor and structure factor determination ("p (q) and s (q) crease"). *JACS Au* **2023**, *3*, 889−904.

(20) Heil, C. M.; Patil, A.; Dhinojwala, A.; Jayaraman, A. Computational reverse-engineering analysis for scattering experiments (crease) with machine learning enhancement to determine structure of nanoparticle mixtures and solutions. *ACS Cent. Sci.* **2022**, *8*, 996−1007.

(21) Wessels, M. G.; Jayaraman, A. Computational reverse-engineering analysis of scattering experiments (crease) on amphiphilic block polymer solutions: cylindrical and fibrillar assembly. *Macromolecules* **2021**, *54*, 783−796.

(22) Wessels, M. G.; Jayaraman, A. Machine learning enhanced computational reverse engineering analysis for scattering experiments (crease) to determine structures in amphiphilic polymer solutions. *ACS Polym. Au* **2021**, *1*, 153−164.

(23) Wu, Z.; Jayaraman, A. Machine learning-enhanced computational reverse-engineering analysis for scattering experiments (crease) for analyzing fibrillar structures in polymer solutions. *Macromolecules* **2022**, *55*, 11076−11091.

(24) Ye, Z.; Wu, Z.; Jayaraman, A. Computational reverse engineering analysis for scattering experiments (crease) on vesicles assembled from amphiphilic macromolecular solutions. *JACS Au* **2021**, *1*, 1925−1936.

(25) Heil, C. M.; Jayaraman, A. Computational reverse-engineering analysis for scattering experiments of assembled binary mixture of nanoparticles. *ACS Mater. Au* **2021**, *1*, 140−156.

(26) Wu, Z.; Jayaraman, A. *arthijayaraman-lab/crease-ga: (v0.0.1)*. (2021).

(27) Burke, E. K.; Gustafson, S.; Kendall, G. Diversity in genetic programming: An analysis of measures and correlation with fitness. *IEEE Trans. Evol. Comput.* **2004**, *8*, 47−62.

(28) Lee, J. Y.; Song, Y.; Wessels, M. G.; Jayaraman, A.; Wooley, K. L.; Pochan, D. J. Hierarchical self-assembly of poly (d-glucose carbonate) amphiphilic block copolymers in mixed solvents. *Macromolecules* **2020**, *53*, 8581−8591.

(29) Ma, Y.; Heil, C.; Nagy, G.; Heller, W. T.; An, Y.; Jayaraman, A.; Bharti, B. Synergistic role of temperature and salinity in aggregation of nonionic surfactant-coated silica nanoparticles. *Langmuir* **2023**, *39*, 5917−5928.

(30) Gupta, N.; Jayaraman, A. Computational approach for structure generation of anisotropic particles (casgap) with targeted distributions of particle design and orientational order. *Nanoscale* **2023**, *15*, 14958−14970.

(31) Akepati, S. V. R.; Gupta, N.; Jayaraman, A. *Data Set of Structural Features and a Few Selected Scattering Profiles and Structures Prepared for CREASE-2D Method*, 2024..

(32) Glatter, O.; Kratky, O. *Small Angle X-Ray Scattering*; Academic Press, 1982.

(33) Guinier, A.; Fournet, G. *Small-angle Scattering of X-Rays, Structure of Matter Series*; Wiley, 1955.

(34) Brisard, S.; Levitz, P. Small-angle scattering of dense, polydisperse granular porous media: Computation free of size effects. *Phys. Rev. E* **2013**, *87*, 013305.

(35) Huang, G.-R.; Wang, Y.; Do, C.; Shinohara, Y.; Egami, T.; Porcar, L.; Liu, Y.; Chen, W.-R. Orientational distribution function of aligned elongated molecules and particulates determined from their scattering signature. *ACS Macro Lett.* **2019**, *8*, 1257−1262.

(36) Huang, G.-R.; Carrillo, J. M.; Wang, Y.; Do, C.; Porcar, L.; Sumpter, B.; Chen, W.-R. An exact inversion method for extracting orientation ordering by small-angle scattering. *Phys. Chem. Chem. Phys.* **2021**, *23*, 4120−4132.

(37) Elasri, M.; Elharrouss, O.; Al-Maadeed, S.; Tairi, H. Image generation: A review. *Neural Process. Lett.* **2022**, *54*, 4609−4646.

(38) Shrestha, R.; Xie, B. Conditional image generation with pretrained generative model. *arXiv* **2023**, arXiv:2312.13253.

(39) McElfresh, D.; Khandagale, S.; Valverde, J.; P. C, V.; Feuer, B.; Hegde, C.; Ramakrishnan, G.; Goldblum, M.; White, C. When do neural nets outperform boosted trees on tabular data? *arXiv* **2005**, arXiv:2305.02997.

(40) Song, K.; Yan, F.; Ding, T.; Gao, L.; Lu, S. A steel property optimization model based on the xgboost algorithm and improved pso. *Comput. Mater. Sci.* **2020**, *174*, 109472.

(41) Choi, D.-K. Data-driven materials modeling with xgboost algorithm and statistical inference analysis for prediction of fatigue strength of steels. *Int. J. Precis. Eng. Manuf.* **2019**, *20*, 129−138.

(42) Gong, J.; Chu, S.; Mehta, R. K.; McGaughey, A. J. Xgboost model for electrocaloric temperature change prediction in ceramics. *npj Comput. Mater.* **2022**, *8*, 140.

(43) Zhang, R.; Li, B.; Jiao, B. Application of xgboost algorithm in bearing fault diagnosis. *IOP Conf. Ser. Mater. Sci. Eng.* **2019**, *490*, 072062.

(44) Chen, T.; Guestrin, C. *Xgboost: A Scalable Tree Boosting System*; Association for Computing Machinery: New York, NY, USA, 2016; pp 785−794.

(45) Thebelt, A.; Tsay, C.; Lee, R.; Sudermann-Merx, N.; Walz, D.; Shafei, B.; Misener, R. Tree ensemble kernels for bayesian optimization with known constraints over mixed-feature spaces. *Advances in Neural Information Processing Systems*; Curran Associates, Inc., 2022; Vol. *35*, p 37401.

(46) Haupt, R. L.; Haupt, S. E. *Practical Genetic Algorithms*; John Wiley & Sons, 2004.

(47) Marsili Libelli, S.; Alba, P. Adaptive mutation in genetic algorithms. *Soft Comput.* **2000**, *4*, 76−80.